ISTITUTO NAZIONALE DI FISICA NUCLEARE

Sezione di Trieste

INFN/TC-93/14

24 agosto 1993

A. Bressan, A. Georgoussis, M. Giorgi, M. Lamanna, A. Martin and A. Piccotti

A MONTE CARLO CODE FOR ANTINEUTRON DETECTORS

Servizio Documentazione
dei Laboratori Nazionali di Frascati

A Monte Carlo Code for Antineutron Detectors

A. Bressan, A. Georgoussis, M. Giorgi,
M. Lamanna, A. Martin.
INFN Trieste and University of Trieste, Italy

A. Piccotti.
INFN Torino and University of Torino, Italy

Trieste, August 24, 1993

Abstract

A description of the antineutron code built up to study the performances of the PS199 ANC detectors is given, together with the physical inputs for the code, and a review of the results.

1 Introduction

The aim of this report is to describe the Monte Carlo code for the antineutron detectors used in the PS199 experiment at LEAR. It is organised as follows: first of all there is a short description of the experimental set-up with some details for the antineutron detectors; then the parametrizations for the various cross-sections are detailed and the simulation procedure is described. At the end an overview of the results is given.

Experiment PS199 took data to measure the angular dependence of the spin observables A_{0n} (at 8 energies, among 600 and 1300 MeV/c momentum of the antiproton incident beam), and D_{0n0n} (at 600 and 900 MeV/c) in the charge-exchange channel $\bar{p}p \to \bar{n}n$. The results for A_{0n} at all energies have been already published ([1] and [2]) as well as the measurement of the charge-exchange differential cross-section at 693 MeV/c [3] and the measurement of D_{0n0n} at 875 MeV/c [4].

The layout of the experiment is shown in fig. 1; the neutron and the antineutron produced in the charge-exchange reaction are detected in the NC and ANC detectors respectively. We have used a polarized pentanol target (PT), working in 'frozen spin mode', for the measurement of A_{0n} and D_{0n0n}, with an average polarization of $\sim 80\%$ during the data taking. For calibration purposes we have collected some data also on a liquid hydrogen target, that can be placed inside the cryostat of the PT. The three NC detectors are made with scintillator counters (BC 412, equivalent to NE 110), 8 cm wide, 20 cm thick and with a length ranging from 40 to 130 cm. The bars are arranged vertically with the smaller ones close to the beam axis, and are viewed from each end by 5' PMs; this allows the measurement of the interaction point along the bar axis (y-coordinate), which is given by the difference from the top and bottom PM's time-of-flight (TOF), and a reduction of the spurious signals asking a top-bottom coincidence. The antineutron detectors (ANCs) are optimized to detect $\bar{n}$'s annihilations. The ANC consists of five identical modules. Each module is made of four planes of limited streamer tubes (LST) with x and y external read-out, which covers an active area of 202×166 cm^2 (horizontal $\times$ vertical). In the middle of each module there is a hodoscope plane, 1 cm thick, made by six vertical scintillator slabs, 33 cm wide and 166 cm long, for trigger purpose and TOF measurement. Also these slabs are viewed by two PMs each, and a hit is given by a top-bottom coincidence. Two walls of aluminium, 6.4 mm thick, close up a module, that is only 155 mm thick. Iron slabs, 3 cm thick, and a surface of 200×166 cm^2, are interleaved between the modules, acting as antineutron absorbers; together with the aluminium of the modules they give 90% of the interaction length of the detector. Due to this most of the antineutrons annihilate in the absorbers, giving a characteristic star pattern in the nearest LST planes; the tracks of the charged particles (mostly pions and electrons from electromagnetic showers of the γ's from π^0 decay) produced in the annihilation are then reconstructed by the off-line analysis.

The beam line used by the experiment is the C1 from LEAR, with a typical intensity of 10^6 antiprotons per second. A complete description of the apparatus

and of the data analysis can be found in ref. [2].

2 Antineutrons identification

The basic philosophy for detecting the $\bar{n}$'s is to reconstruct by the LSTs the tracks of the charged particles coming from the annihilation in one of the four iron slabs, where about 85% off the material of the detector is concentrated (the structure is modular in order to increase the detecting efficiency by increasing the annihilation probability).

The iron slab thickness was chosen as a compromise among these three conditions:

- large $\bar{n}$ annihilation probability;
- large γ (from π^0 decay) conversion efficiency;
- small absorption of charged pions.

An antineutron is identified by requiring in the off-line analysis a 'star' pattern in one of the ANC detectors, i.e. at least three tracks in one projection of the ANC (xz or yz), meeting within well defined tolerances in a single point inside one iron slab; on the other projection at least two tracks, crossing in the same iron slab are required. As a consequence, we need three or more charged particles coming out from the absorber, and the multiplicity of the annihilation products is a critical point for the antineutron identification. Thus a crucial point in the development of the simulation program is the description of the annihilation. The $\bar{N}N$ annihilation data show that on average five pions are produced (with on average two π^0), but, when the annihilation occurs inside a nucleus, final state interactions can alter the multiplicity. The CERN standard package for detectors' developments and Monte Carlo simulations GEANT [5] works in the 'impulse approximation' (annihilation on a single nucleon in the nucleus) and does not take into account, for example, the Fermi motion of the nucleon and nuclear cascades that can be initiated by pions in the nuclear matter. Moreover, the nuclear processes are not well known in the low energy range of this experiment and the parametrizations of the hadronic cross-sections are not accurate enough below 2 GeV. To overcome these problems we have built up a Monte Carlo starting from the Infra Nuclear Cascade code (INC) developed by Iljinov et al. [6, 7], that simulates all the inelastic antinucleon-nucleon interactions inside the nucleus; in addition we have used recent LEAR cross-sections data (both $\bar{N}N$ and $\bar{N}A$).

The Monte Carlo can be used to solve most of the problems connected with the antineutron detectors and with the data-taking setup. These are:

- ANC efficiency as a function of the $\bar{n}$ topology;
- γ contamination (i.e. detection efficiency for photons);

- energy dependence of the antineutron reconstruction efficiency;
- edge effects on reconstruction efficiency;
- smearing effects in the charge-exchange $\frac{d\sigma}{d\Omega}$ measurement;
- overall efficiency of the ANCs with our data taking set-ups.

The program can also be used for

- optimization of ANC geometry;
- tests of the off-line reconstruction program;

although historically it was not used for these purposes due to the very long tuning time the full program has required.

Some of the previous items need few words of explanation. By edge effect we mean the variation of efficiency as a function of the distance from the annihilation point and the border of the ANC detector. The smearing effect is the distortion of the measured angular distribution due to elastic and inelastic interactions of the $\bar{n}$'s in the NC detector located before the ANC. A good estimate of the smearing corrections is quite important for an accurate measurement of the differential charge-exchange cross-section. In section 5 we describe the results of the Monte Carlo simulation for some of these points.

3 Input of the antineutron code

In the first paragraph of this section we give the used parametrization for the antineutron total and differential cross-sections in the different materials (Fe, Al, CH of the organic scintillator...); in the second one a brief description of the annihilation process itself. Finally we give the cross-section for the interactions of charged pions produced in the annihilation and we recall all the electromagnetic processes considered by the EGS Package [8], which is used to simulate the interactions of the photons coming from the π^0 decay.

3.1 Antineutron cross sections

The only existing measurement of low energy $\bar{n}$-nucleus annihilation cross-section, is the one on iron from ref. [9], whose data have been parametrised as a function of energy as:

$$\sigma_{an}(\bar{n}, Fe) \cong \left(891 + \frac{233}{p_{\bar{n}}}\right) \qquad p_{\bar{n}} \text{ in GeV}/c, \quad \sigma_{an} \text{ in } mb \tag{1}$$

The extension to other nuclei is made assuming a $A^{2/3}$ dependence from the atomic mass number; so we have:

$$\sigma_{an}(\bar{n}, A) = \left(61 + \frac{16}{p_{\bar{n}}}\right) \cdot A^{2/3} \tag{2}$$

To describe the antineutron interaction with the hydrogen nucleus, a different parametrization is used, according to the data of ref. [10]:

$$\sigma_{an}(\bar{n}, H) = \left(41.4 + \frac{29.0}{p_{\bar{n}}}\right) \tag{3}$$

No elastic cross-section data exists, but, looking at $\bar{p}p$ data (see for instance [11]), we can put with a realistic approximation:

$$\sigma_{el}(\bar{n}, A) = \frac{1}{2}\sigma_{an}(\bar{n}, A) \tag{4}$$

We have taken the $\bar{n}$ differential cross-section equal to the $\bar{p}$ elastic cross-section of ref. [12], which we have parametrized as a superposition of two gaussians:

$$\frac{d\sigma}{d\theta^2} = \beta \cdot e^{-b\theta^2} + \alpha \cdot e^{-a\theta^2} \tag{5}$$

where:

$$\begin{aligned} \beta &= 82 \times A^{c_1} \times p_{\bar{n}}^{c_2} \quad & c_1 &= 1.50 \quad & c_2 &= -0.2 \\ b &= 19 \times A^{c_3} \times p_{\bar{n}}^{c_4} \quad & c_3 &= 0.67 \quad & c_4 &= 1.85 \\ \alpha &= 0.0013 \times \beta \quad & a &= 0.12 \times b \end{aligned}$$

and $p_{\bar{n}}$ in GeV/c. This expression overestimates a bit the elastic cross-section at large scattering angles: in this way we take into account also the effect of inelastic $\bar{n}$-nucleus scattering (important at large angles), not parametrized in the Monte Carlo.

3.2 The Intra Nuclear Cascade code

As mentioned in section 2, the $\bar{n}$ annihilation on nuclei is simulated with the INC code of Iljinov et al which is recommended for energies up to 10 GeV. This cascade model is a refined tool to describe the $\bar{N}$-nucleus processes. It takes into account the distortion given by the Fermi motion, and the pions produced in the annihilation can also interact in the nuclear matter. This can lead to thermalized nuclei production and a subsequent de-excitation of the residual nucleus through evaporation and multifragmentation, and alters both the pion energy spectrum and the mean pion number. The basic assumptions of the INC model are the following [7]:

1. inelastic hadron-nucleus interactions are a succession of independent collisions of primary and fast secondary particles with nucleons;

2. the pion multiplicity in $\bar{N}N$ annihilation is generated according a statistical model [13];

3. the particles involved in the cascade are treated as classical, and any interaction between them is neglected;

4. the cross-sections for elementary collisions are the same as in vacuum, except that the Pauli exclusion principle prohibits the transition of the cascade nucleons into states that are filled with intranuclear nucleons.

The nucleus is described as a mixture of degenerate Fermi gases of neutrons and protons, confined in a spherical potential well. The momentum distribution of the nuclear nucleons is given in the local Fermi-gas approximation.

The code we use takes into account only annihilations with uncorrelated pions in the final state, neglecting strange particles productions and intermediate channels with heavy mesons such as ρ and ω. Also the nuclear fragments, necessary for a detailed energy balance of the reaction, lose their importance in the successive steps of our simulations. Protons, deuterons, α particles or bigger fragments can cross only small absorber thicknesses, due to their short range at these energies, and don't come out of the iron plate. Also neutral fragments, such as neutrons, are not treated by our code since in most of the cases they don't give any signal either in the LSTs or in the scintillator planes.

In fig. 2 we show the energy distributions of charged pions for incident antineutrons ranging from 'at rest' up to 1500 MeV/c (the distributions for neutral pions are essentially the same). All the distributions show an almost identical shape, with a peak around 200 MeV of total energy, and a long tail that extend up to $\sim$ 1 GeV. For higher incoming $\bar{n}$ momenta is also visible a small bump at an energy ($\sim$ 300-400 MeV), that slowly increases while increasing the $\bar{n}$ momentum. The low energy peak is mainly due to pions that undergo nuclear reactions and start nuclear cascade, losing almost all their kinetic energy. The bump is located around the average energy for pions produced by annihilations on free nucleons. The pion multiplicity for annihilation on iron, at different $\bar{n}$ momenta (among 100 and 1500 MeV/c) is presented in fig. 3, while the mean values are shown in table 1. The multiplicity changes weakly in our energy range. Furthermore, we can notice that there is a small decrease of the average pion number around 500 MeV/c. Figure 4 shows the angular distribution of the charged pions with respect to the $\bar{n}$ line-of-flight at different energies. It is interesting to note that a forward-backward asymmetry is present also for annihilation at rest, indicating that annihilation is a surface mechanism: only forward going pions, that cross the nuclear matter interact with the nucleons; at higher energies the Lorentz boost stretches the distribution toward the forward direction. The integrated forward-backward asymmetry for neutral and charged pions is given in table 2.

$p_{\bar{n}}$ GeV/c	mean pion multiplicity					
	at annihilation point			out of iron plate		
	$\pi^{\pm}$	π^0	total	$\pi^{\pm}_{out}$	$e^{\pm}_{out}$	total
0.10	2.45	1.78	4.23	1.47	2.55	4.02
0.25	2.41	1.79	4.20	1.42	2.51	3.93
0.50	2.38	1.76	4.14	1.43	2.38	3.81
0.75	2.39	1.82	4.21	1.42	2.63	4.05
1.00	2.45	1.85	4.30	1.49	2.60	4.09
1.25	2.52	1.92	4.44	1.54	2.75	4.29
1.50	2.59	1.99	4.58	1.59	2.92	4.51

Table 1: Mean pion and electron multiplicity as a function of the incoming antineutron momentum. The first three columns show the number of charged and neutral pions given by the annihilation on iron from the INC code. Columns four to six give the charged particles multiplicity, for particles that come out from the absorber slabs.

forward - backward asymmetry						
$p_{\bar{n}}$ GeV/c	π^0		$\pi^{\pm}$		γ	
	forward	*backward*	*forward*	*backward*	*forward*	*backward*
at rest	46.65	53.35	47.03	52.97	48.27	51.73
0.25	49.04	50.06	49.40	50.60	50.02	49.08
0.50	52.95	47.05	53.51	46.49	53.36	46.64
0.75	56.81	43.19	57.89	42.10	55.75	44.25
1.00	60.40	39.60	61.41	38.59	58.66	41.34
1.25	63.16	36.84	64.01	35.99	60.38	39.62
1.50	64.52	35.48	65.95	36.05	60.98	39.02

Table 2: Asymmetry in neutral, charged pions and photons angular distribution with respect to the $\bar{n}$ line-of-flight.

3.3 Neutral pions

Neutral pions have a very short life-time (8.4×10^{-17} s), and also at the maximum energy of the pion spectrum, the decay path is of the order of 1.3 μm. Therefore we can assume that they decay in two γ's just at the $\bar{n}$ annihilation point. The simulation of the γ's interactions with our apparatus is made by means of the standard EGS code developed at SLAC. This package, applicable to γ's from a few keV up to 30 GeV, reproduces all the main characteristics of the cascade development and contains a full set of programs where the cross-sections, necessary to the simulation, are computed for all materials.

The different processes simulated in the code are the following: concerning photons we have

- *Compton scattering*;
- *pair production*;
- *photoelectric effect*;

while for electrons the following processes are considered:

- *multiple scattering*;
- *positron annihilation*;
- *Bhabha scattering*;
- *Møller scattering*;
- *bremsstrahlung*.

Cuts on electrons and γ's energies must be set in the data cards of the code. We choose to cut below 0.4 MeV and 0.9 MeV for photons and electrons respectively.

In fig. 5 we can see the energy distribution of the photons for 500 MeV/c incoming $\bar{n}$ momentum, that essentially reproduces the trend of the pion spectra. Figure 6 shows the distribution of the distance between the photons' creation point (i.e. the $\bar{n}$ annihilation point) and their conversion point projected along the axis of the detector. The large peak at $\Delta z = 0$ is due to photon conversion in the same iron plate where the $\bar{n}$ annihilates; the others peaks come from conversions in the scintillator plane (Δz =8 cm) and in the nearest iron absorbers (Δz =19 cm).

3.4 Charged pions

To take care of the charged pion interactions in the detector, elastic, inelastic, absorption and charge-exchange nuclear cross-sections are considered; they are evaluated by means of a linear interpolation of the existing π^+ and π^- data at different energies [14]. The nuclear interaction probability is calculated using:

$$P_{int} = 1 - e^{-\alpha r} \tag{6}$$

$$\alpha = \sigma_{tot}(E) \cdot N_{AV} \cdot \rho / A,$$

then, the type of interaction is selected.

For the differential elastic cross-section the following parametrization is used [15]:

$$\frac{d\sigma}{dt} \propto e^{1.44 \cdot A^{2/3} \cdot t / 4 \cdot 197^2}, \qquad t = 2p^{*^2}(cos\theta^* - 1). \tag{7}$$

The scattering angle in the center-of-mass system is evaluated using the standard kinematical relations; the laboratory scattering angle is obtained by means of a Lorentz transformation from the πN center-of-mass system (interaction with only one nucleon of the nucleus), and without taking into account the Fermi motion.

The differential inelastic cross-section is given by [16]:

$$\frac{d\sigma}{dt} \propto e^{t/8 \cdot \pi \cdot \sigma_{in} \cdot 1.97^2} \tag{8}$$

The scattering angle in the laboratory system is evaluated, taking into account the mass of the nucleus since the inelastic process is supposed to interest the whole nucleus and not only one nucleon, as for the elastic scattering.

The charge-exchange differential cross-section of $\pi^{\pm} A \rightarrow \pi^0 X$ is given in the approximation of pure pion-nucleon interaction, using the parametrization of ref. [17]:

$$\frac{d\sigma}{d\Omega^*} = \sum_{j=1}^{4} c_j \cdot \cos^j \theta^* \tag{9}$$

with the values of the coefficients c_j that are evaluated by a fit of the data.

Electromagnetic interactions are treated as a continuum process and not as single scattering events. We take into account multiple scattering and energy loss by ionization, step by step, with a step size (different for the various materials) that is of the order of ~1% of the total nuclear interaction probability; as an example this roughly corresponds to a millimeter step path in iron. The energy loss of charged pions by ionization is evaluated according to the classical Bethe-Bloch formula:

$$\left(\frac{dE}{dX}\right)_{ion} = \frac{D \cdot Z_{med} \cdot \rho_{med}}{A_{med}} \cdot \left(\frac{Z_{inc}}{\beta}\right)^2 \left[\ln\left(\frac{2 \cdot m_e \cdot \gamma^2 \cdot \beta^2 \cdot c^2}{I}\right) - \beta^2\right] \tag{10}$$

where:

$$D = 4 \cdot \pi \cdot N_{AV} \cdot r_e^2 \cdot c^2$$

Z_{med} and A_{med} are atomic and weight numbers of the material, ρ_{med} is the density, m_e is the electron mass, and I is the *ionization constant.* The angle of multiple scattering is generated in the two projections (xz and yz) according to a gaussian distribution, with a width given by:

$$\theta_o = \frac{14.1(MeV/c)}{p \cdot \beta} \cdot Z_{inc} \cdot \sqrt{\frac{L}{L_R}} \cdot \left[1 + \frac{1}{9} \cdot \log_{10}\left(\frac{L}{L_R}\right)\right] \tag{11}$$

where L_R is the radiation length and p is the pion momentum. The value of the pion momentum p is randomly chosen between its initial and final value in the moving step.

4 The Monte Carlo code

The code is made with five different programs, and all the informations are transferred from one to others by means of six files. The flow diagram is displayed in fig. 7; the routines are the rounded boxes and the output-input files are the square boxes. At the end of the program chain we are left with one file (shown with EPIO FILE in the previous figure), where data are decoded with the same format of experimental ones. All the different steps of the simulation (ANTNEF, PANEGS and PANCLU) use the same ANC geometry that is shown in fig. 8. It is also possible to turn on and off the presence of the NC detector in front of the antineutron counter, taking into account or not $\bar{n}$ interaction with the hydrogen and carbon nuclei of this detector.

The ANTNEF program generates the incoming antineutrons according one of the following choices:

- *orthogonal to the ANC and in its centre*;
- *orthogonal to the detector and uniformly distributed over the whole surface*;
- *isotropically emitted from the target;*
- *emitted from the target, according to* $\left(\frac{d\sigma}{d\Omega}\right)_{\bar{p}p\to\bar{n}n}$ *in the angular range covered by the ANC.*

For the first three options, the $\bar{n}$ momentum is fixed inside one simulation, while for the forth one, we give the $\bar{p}$ beam momentum, and the $\bar{n}$ momentum is evaluated from the generated scattering angle.

ANTNEF simulates all the $\bar{n}$ interactions with the ANC and NC detectors. If an antineutron annihilates inside a counter, the program reads from the INC file the number of produced pions together with their direction, momentum and charge; neutral pions immediately decay into photons. This closes the first step of the simulation. All the informations about pions and photons are written in the input file for PANEGS and PANCLU, together with the antineutron annihilation position. In table 3 we show the results of one ANTNEF simulations for a beam of antineutrons incoming in the ANC centre and without the NC in front of the $\bar{n}$ detector. As we can see most of the antineutrons stop in the ANC counter and most of these annihilations ($\sim 80\%$) take places inside the absorber plates. On the other hand $\sim 25-30\%$ of $\bar{n}$'s undergo an elastic scattering in the ANC, before annihilating.

The distribution of $\bar{n}$ annihilation points along the z direction with and without the NC is presented in fig. 9 and fig. 10 respectively; in both the cases the momentum of the incoming antineutrons is 500 MeV/c. They show the exponential behaviour due to absorption.

The PANEGS code is based on the EGS package and simulates the electromagnetic shower development. When a charged particle of the shower (namely $e^{\pm}$)

$p_{\bar{n}}$ GeV/c	annihilations (%)						
	total annihi.	annih.with elastic sc.	absorbers				total absorbers
			1°	2°	3°	4°	
0.10	99.36	32.98	53.65	15.62	3.84	0.67	73.78
0.25	93.74	30.80	40.43	21.42	10.67	3.98	76.50
0.50	86.54	26.42	35.61	22.66	13.85	8.63	80.75
0.75	82.64	25.40	33.76	22.82	14.71	9.92	81.21
1.00	80.71	23.80	32.80	22.31	15.09	10.32	80.52
1.25	78.95	23.67	31.79	23.05	15.37	10.67	80.88
1.50	78.26	23.10	31.50	23.30	15.44	10.74	80.98

Table 3: Annihilation probability in the ANC for different incoming $\bar{n}$ momenta. We can notice that about 80 % of the annihilations are on the absorbers

crosses an active layer of the apparatus the code recorded the hit position. On average 1.25 charged particles ($e^{\pm}$) come out of the iron thickness for each π^0. Pair creation from γ helps considerably the star pattern reconstruction; as we can see in table 1, on average less then two charged pions per event come out from the absorber, while more than two electrons give a signal in the nearest LST plane. If we switch off the electromagnetic particles from the simulation the 'star' reconstruction efficiency decreases of about 70%. Indeed, we chose thick iron as absorber just to pull on the γ conversion probability.

Finally, the PANCLU program simulates the passage of charged pions through the different media of the counter. As mentioned before, nuclear interactions as absorption, inelastic, elastic and pion charge-exchange are taken into account together with the electromagnetic processes. The hit of a charged pion with LST planes and scintillator hodoscopes is then recorded. The conversion from a hit to a x and y cluster of strips is made at this level. The cluster size is given according the experimental distributions measured with cosmic rays [18] that depend on the θ_x and θ_y angles of the particle. The efficiency of the LST (measured to be of the order of $\sim$ 87-90%) is also taken into account in the simulation.

In table 1 we show the mean number of pions and electrons coming out from the iron plate, together with starting multiplicity.

At the end READWR builds a suitable output file for the off-line reconstruction program using the EPIO CERN standard to allow the transfer of the data on different computers. The code has been written in Fortran 77 and typically runs on Vax machines. Generally it needs on average about 1.0 sec. for the generation of a complete event on a VAXstation 4000-60.

5 Results

As mentioned in section 1 and 2, the $\bar{n}$ off-line identification is performed first by reconstructing the trajectories of the charged products of the $\bar{n}$ annihilation and then looking for the common origin of these tracks. Fig. 11 shows a display of a Monte Carlo event reconstructed by the off-line analysis; the open circles are the hits on the LST planes and the full rectangles are the fired scintillators. The segments are the reconstructed trajectories and the cross is the computed annihilation point. The 'star' topology of the $\bar{n}$ annihilation event is very clear, and the off-line analysis reconstruct with a good precision the annihilation vertex.

5.1 ANC efficiency

The antineutron stars reconstruction efficiency of the off-line program is easily evaluated from the ratio between the number of stars found and the total number of $\bar{n}$ annihilations generated in the ANC by the Monte Carlo. Bearing this in mind, we can study some basic aspects of our detector: first of all the dependence of the ANC efficiency from the thickness of the iron absorber. We have used a simplified ANC geometry with only one absorber and two modules, and generated a monochromatic $\bar{n}$ beam orthogonal in the centre of the structure. The result of the simulation is shown in fig. 12 for 500 MeV/c incoming $\bar{n}$'s. The different curves are: P_a, i.e. the annihilation probability in the counter; P_r, the reconstruction probability, and $\varepsilon^1_{ANC} = P_a \cdot P_r$, that is the efficiency of the simplified ANC structure. As we can see, between 1 and 3 cm of iron thickness, the reconstruction efficiency P_r increases with the increasing of the thickness and then starts decreasing. The explanation is that for a few centimeters thickness the absorption of charged pions is compensated by the probability of conversion of photons coming from the π^0 decay (which increases with the thickness) while, by increasing the iron thickness, the absorbtion is dominant also in these processes. Knowing ε^I_{ANC}, the efficiency of the full ANC structure (ε_{ANC}) with the four absorbers and the five modules, can then be evaluated. For the full ANC counter the efficiency reaches its maximum value for 3 cm iron thickness. This evaluation has been done for an $\bar{n}$ momentum of 500 MeV/c, but the result depends only slightly on the momentum.

The second important question we would like to answer by the Monte Carlo is the reconstruction probability, and more generally the efficiency of the whole detector as a function of the incoming $\bar{n}$ momentum. Again we generate $\bar{n}$'s which hit the ANC orthogonally in the centre, with the momentum increased in step of 100 MeV/c. The result of this simulation is shown in fig. 13; P_a is the annihilation probability inside the ANC, P_r is the reconstruction probability, and ε_{ANC} is the product of the previous quantities. As we can see, the dependence of P_r from the $\bar{n}$ momentum is very small over the whole energy range. This is expected since the topology of the annihilation events only slightly changes in our $\bar{n}$ momenta range. The pion multiplicity in fact (table 1) is almost constant, and the stretching of the

angular distribution of the charged products in the forward direction (see fig. 4), that raises the density of the hits in the forward hemisphere is not important for the reconstruction efficiency. The reconstruction probability with the standard $\bar{n}$ definition is about 35%. The slope of the ANC efficiency ε_{ANC} is therefore mainly given by the annihilation probability P_a.

5.2 Geometrical acceptance

Using a monochromatic $\bar{n}$ beam, uniformly distributed on the whole ANC, we can evaluate the geometrical acceptance of the detector (needed for the measurement of the differential cross-section) and the dependence of the reconstruction efficiency as the distance between the $\bar{n}$ annihilation point and the detector border. The result of the simulation is shown in fig. 14; the acceptance increases quite fast up to 30 cm from the border, where it practically reaches the full value. The solid curve is a fit of the points using a dependence of the following form:

$$\varepsilon(r) = \frac{\varepsilon_0}{1 + e^{(\frac{\alpha - r}{\beta})}}$$

where r is the distance from the annihilation point to the edge of the detector, ε_0 the reconstruction efficiency in the ANC centre, α and β the fitted parameters ($\alpha = 54$ cm, $\beta = 49$ cm).

5.3 ANC response for γ's

The ANC detector is expected to be sensitive also to high-energy γ-rays. In the experiment γ's from $\bar{p}$ annihilations into neutrals are rejected

1. at the trigger level by a suitable veto-box (sandwich of scintillators and 1.3 Pb radiation length) surrounding the target from all sides except for the incoming beam direction,
2. in the off-line analysis by time-of-flight cuts.

Still, we have investigated with the Monte Carlo the response of the detector for γ's. An incoming γ beam and to reproduce the electromagnetic cascade in the detector are simulated; the result is shown in fig. 15 for γ's energies between 100 and 1000 MeV. The slope of the distribution is given by the fast raise of the average number of $e^{\pm}$ coming out both from the absorber in which the photon showers and from the following one. The electromagnetic cascades are in fact forward peaked and we can imagine that a star topology is reproduced by one or more charged particles that come out from the first absorber and shower again in the next one, giving two or more tracks after it. This can be seen in fig. 16 in which are given both the distribution along the z-axis of the γ conversion point and of the reconstructed star vertex for 500 MeV γ's. For 100 MeV photons, on average, less then half a

particle comes out from the iron in which the γ showers, while at 300 MeV we have on average more than one particle out both from the iron in which the γ convert and from the following one. The detection efficiency for high energy γ ($\geq$ 500 MeV) is rather high, but more than 80 % of the photons produced in $\bar{p}$ or $\bar{n}$ annihilation have an energy lower then 200 MeV and the overall reconstruction efficiency, using the distribution of fig. 5, is about only 5%.

6 Conclusions

The realization of the Monte Carlo code has required a large amount of work but, at the end, we have a very efficient and versatile program, that turns out to be very useful to investigate many aspects connected to antineutron detection.

7 Acknowledgements

We would like to acknowledge the PS199 collaboration and particularly F. Bradamante for the continuous discussions and the very useful suggestions. We would like to thank A. Iljinov and Y. Golubeva for the INC code and useful explanations.

References

[1] R. Birsa et al., *Phys. Lett.* **B 273** (1991) 533.

[2] R. Birsa et al., *Nucl. Phys.* **B 403** (1993) 25.

[3] R. Birsa et al., *Phys. Lett.* **B 246** (1990) 267.

[4] R. Birsa et al., *Phys. Lett.* **B 302** (1993) 517.

[5] R. Brun et al., *GEANT3,* DD/EE/84-1 (1987).

[6] A. S. Iljinov et al., *Nucl. Phys.* **A 382** (1982) 378.

[7] Y. Golubeva et al., *Nucl. Phys.* **A 483** (1988) 539.

[8] R. L. Ford and W. R. Nelson, *EGS3,* SLAC rep. 210 (1978).

[9] M. Agnello et al., *Europhys. Lett.* **7 (1)** (1988) 13.

[10] T. Amstrong et al., *Phys. Lett.* **D 36** (1987) 659.

[11] F. Myhrer, *Nucl. Phys.* **A 508** (1990) 513.

[12] D. Garreta et al., *Phys. Lett.* **B 149** (1987) 659.

[13] S. Orfanidis and V. Rittenberg, *Nucl. Phys.* **B 59** (1973) 570.

[14] D. Ashery et al., *Phys. Rev.* **C 23** (1981) 2173.

[15] C. Chiu et al., *Phys. Rev.* **161** (1967) 1563.

[16] V. D. Barger and B. D. Cline, *Phenomenological Theories of High Energy Scattering*, W. A. Benjamin inc. Publishers, New York, 1969.

[17] R. Jenefsky et al., *Nucl. Phys.* **A 290** (1977) 407.

[18] R. Birsa et al., *Nucl. Inst. Methods* **A 300** (1991) 43.

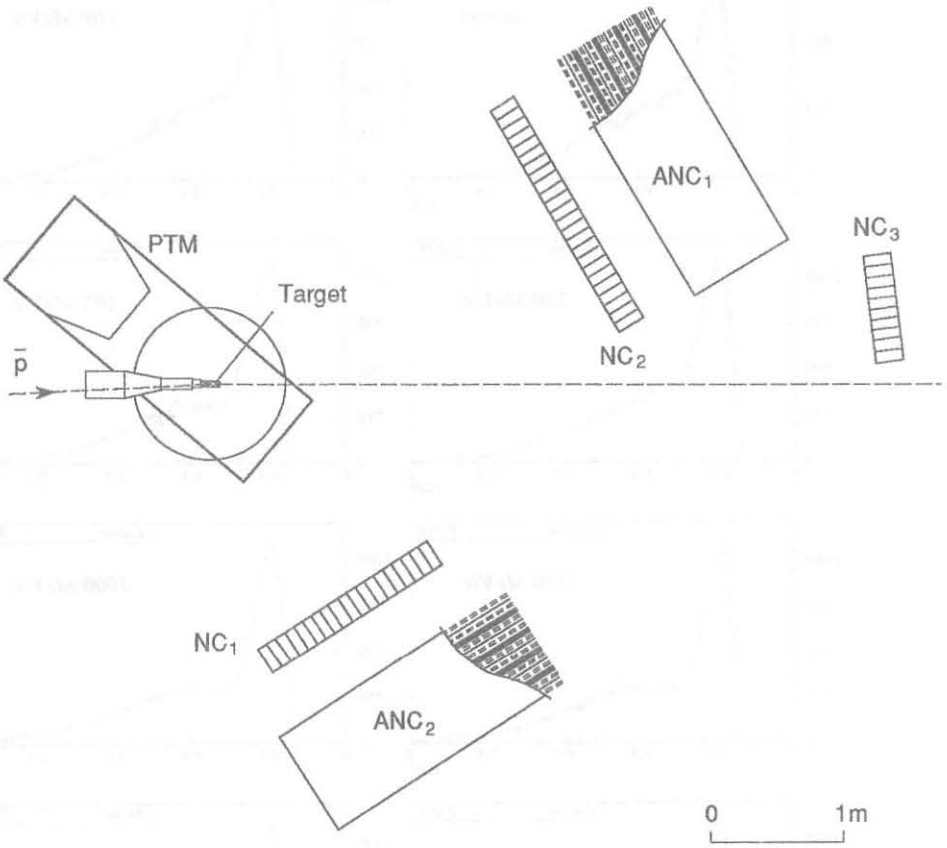

Figure 1: PS199 set-up, ANC and NC are the antineutron and neutron detectors. The target complex is also shown, the dashed line is the incoming and outgoing beam direction.

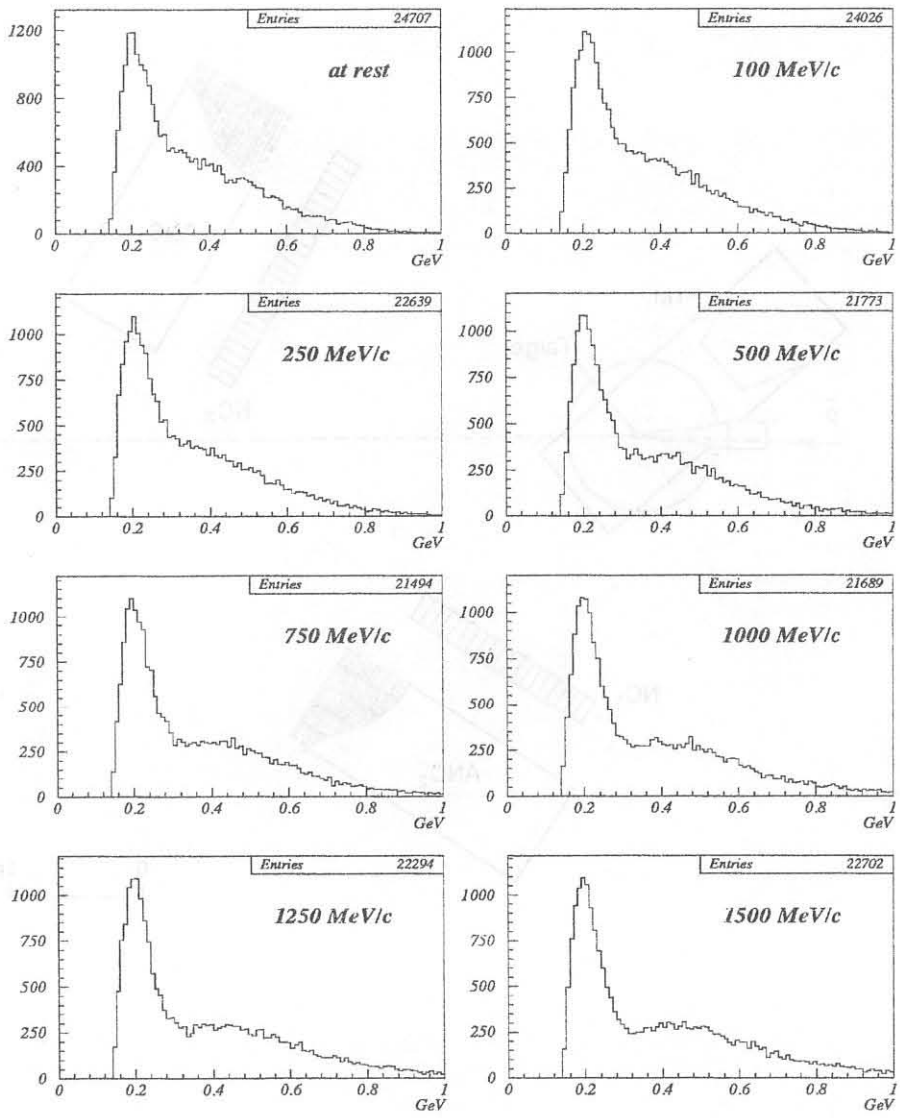

Figure 2: Energy distribution of charged pions coming from the $\bar{n}$ annihilation on iron, at different antineutron momenta.

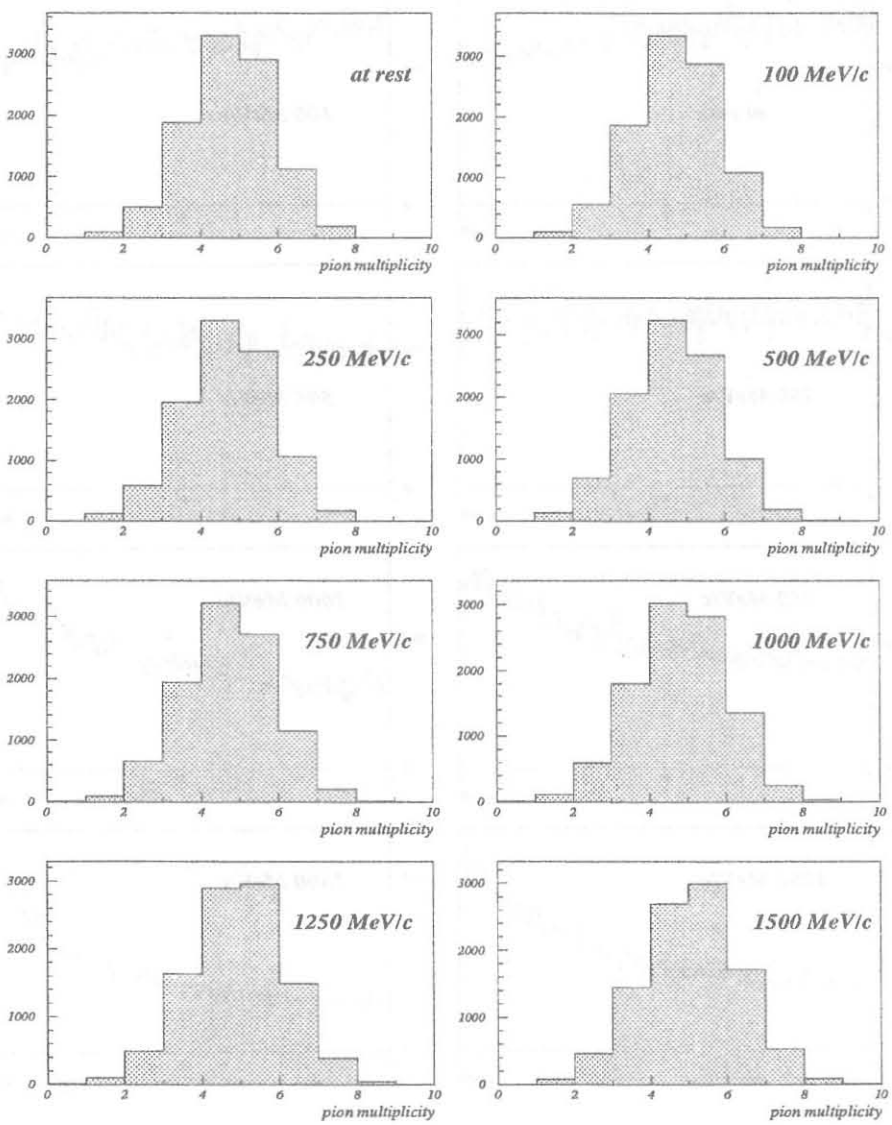

Figure 3: Multiplicity of charged pions coming from the $\bar{n}$ annihilation on iron, at different antineutron momenta.

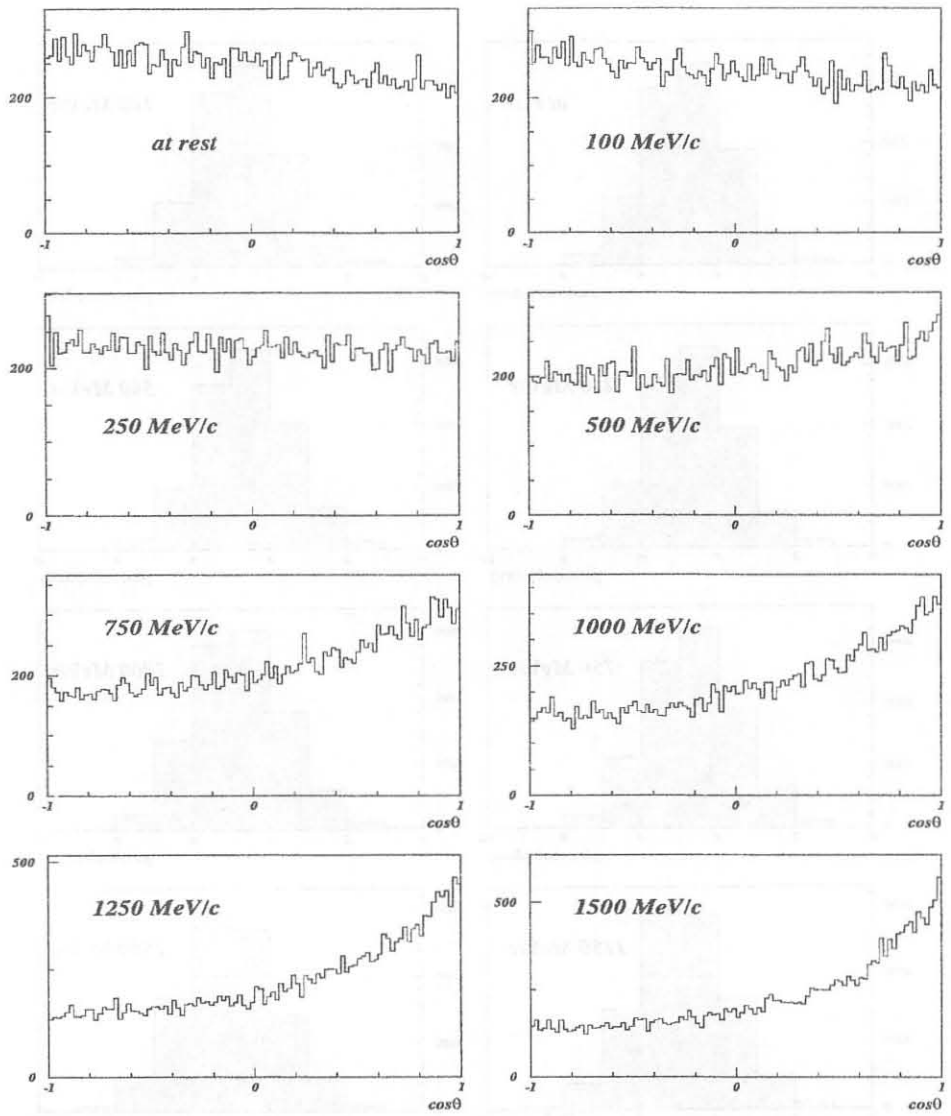

Figure 4: Charged pions angular distribution for different antineutron momenta as a function of the angle θ between the incoming $\bar{n}$ line-of-flight and the outgoing π's, created by the $\bar{n}$ annihilation on iron.

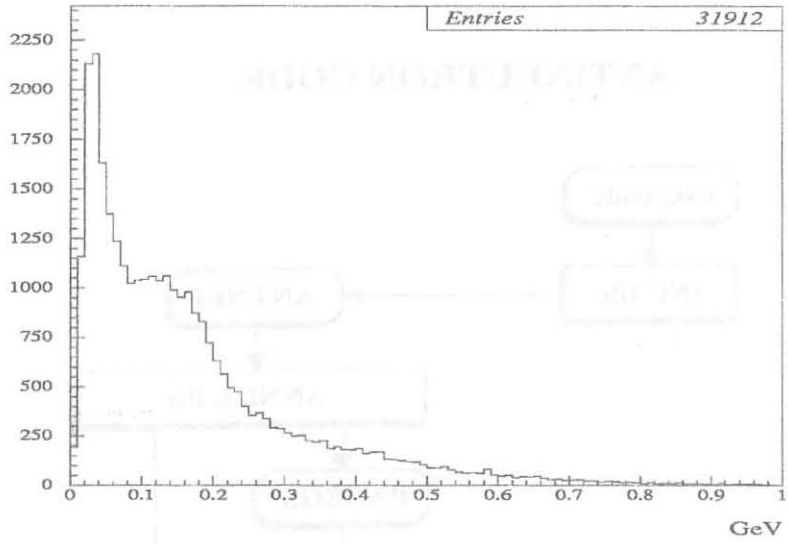

Figure 5: Energy distribution of photons generated by π^0 decay. The momentum of the antineutrons for this simulation was 500 MeV/c.

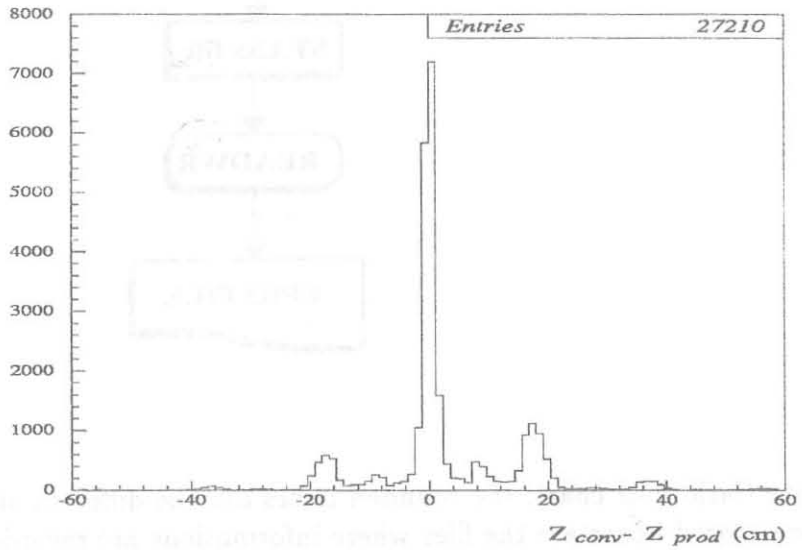

Figure 6: Distance from the γ creation and conversion points along the z axis. The large peak at $\Delta z = 0$ is due to γ's conversion on the same absorber where the $\bar{n}$ annihilates. The smaller peaks are located from conversion on the scintillators (Δz = 8 cm) and nearest irons (Δz = 19 cm).

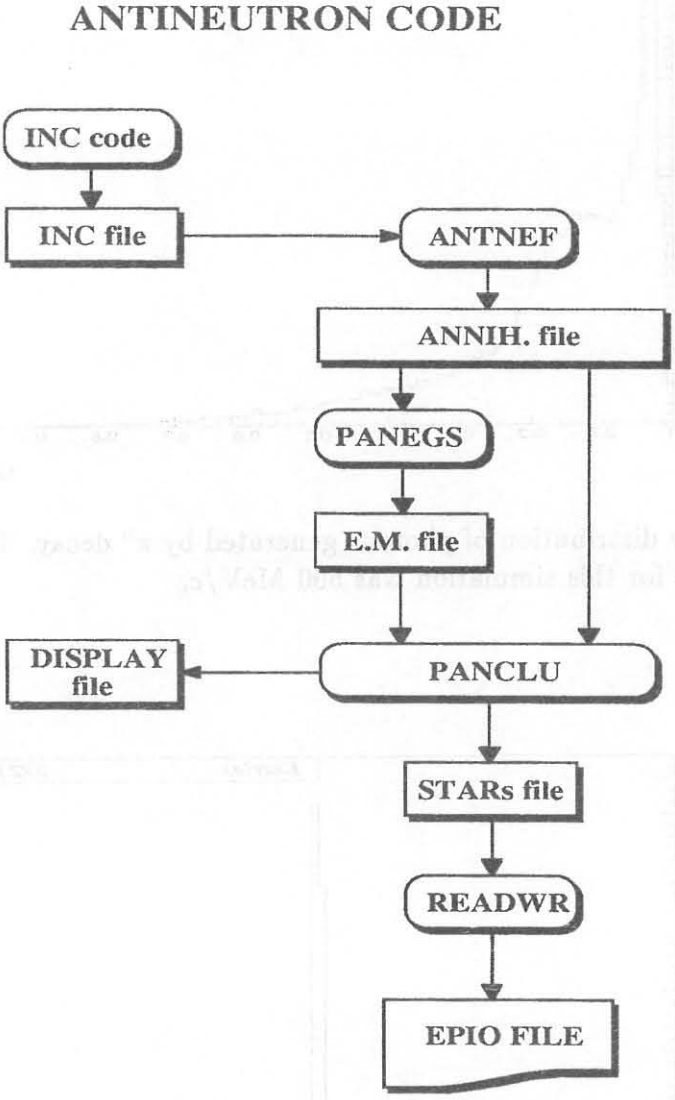

Figure 7: Monte Carlo flow chart; the rounded boxes are the different steps of the simulation, the squared boxes are the files where informations are recorded.

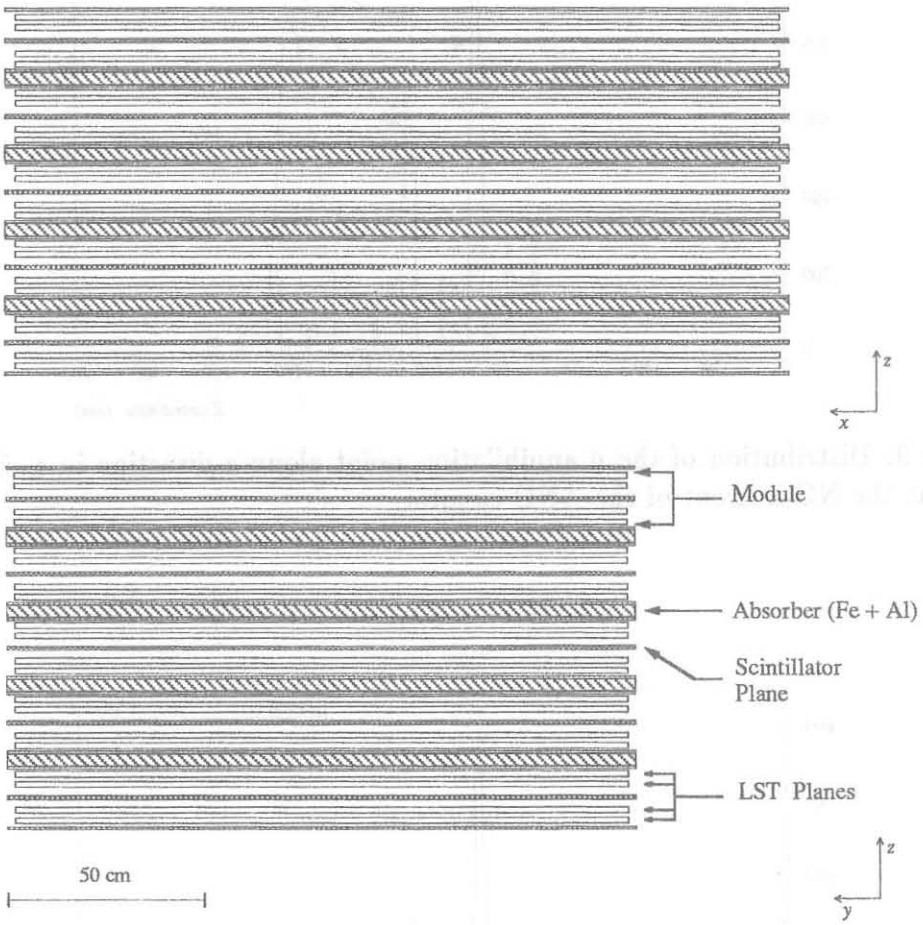

Figure 8: Antineutron counter geometry.

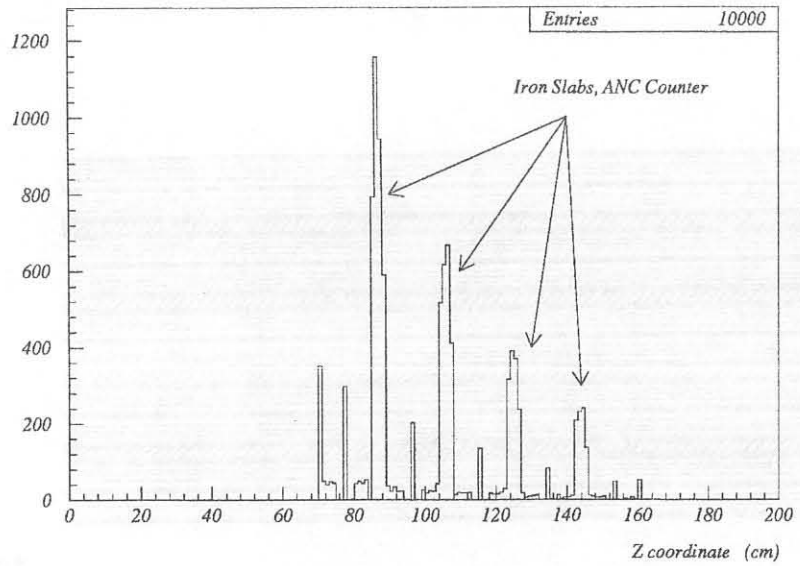

Figure 9: Distribution of the $\bar{n}$ annihilation point along z-direction in a simulation without the NC in front of the ANC counter.

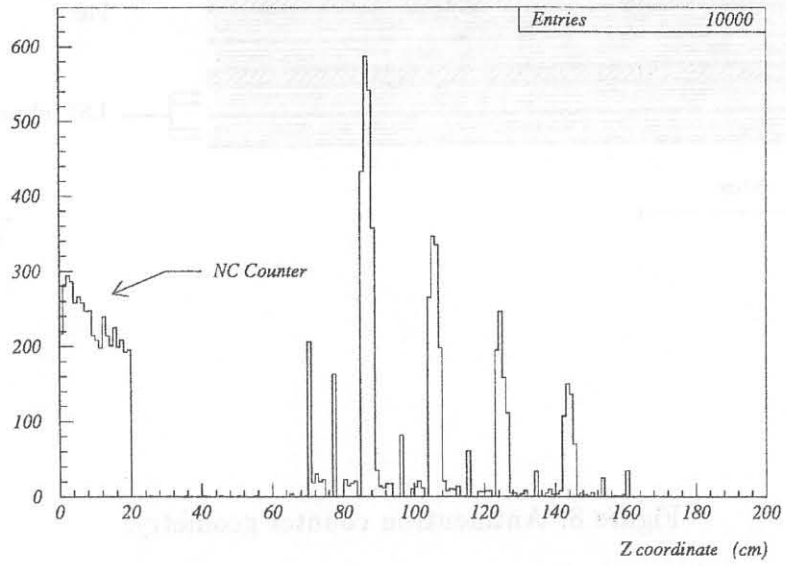

Figure 10: Distribution of the $\bar{n}$ annihilation point along z-direction in a simulation with the NC in front of the ANC counter; about 40% of the annihilations take place in the NC.

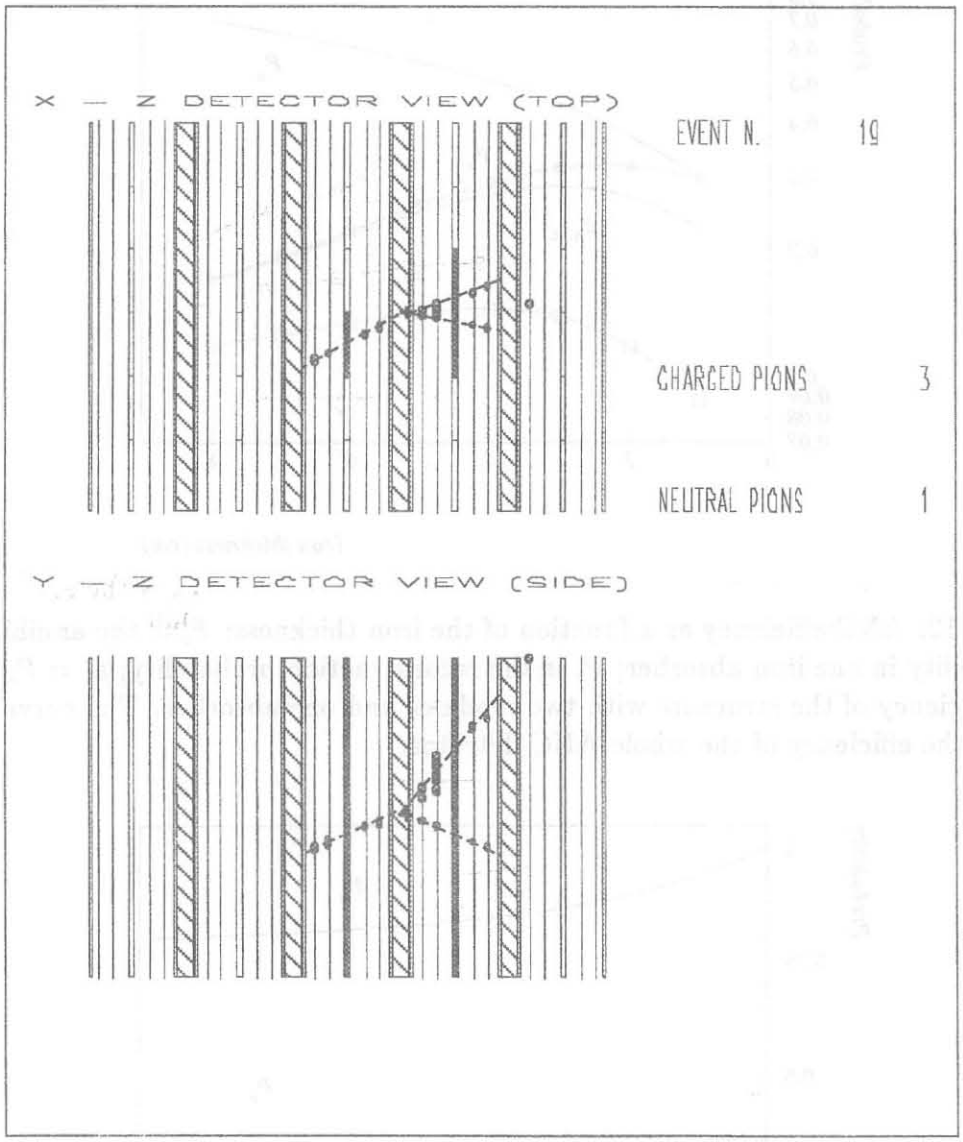

Figure 11: Display of a Monte Carlo event. The black cross is the $\bar{n}$ annihilation point; the black points are the hits on the LST planes, while fired scintillators are shadowed. The dashed lines are the tracks as reconstructed by the off-line program.

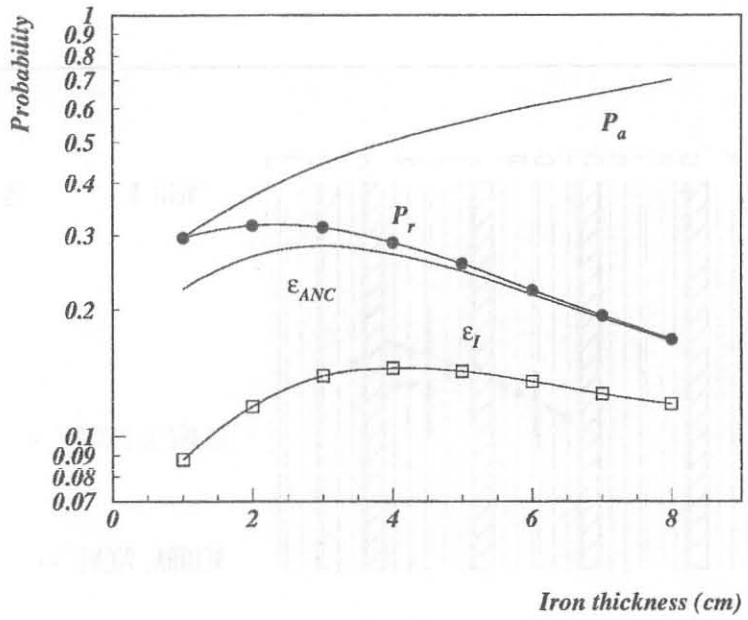

Figure 12: ANC efficiency as a function of the iron thickness: P_a is the annihilation probability in one iron absorber; P_r is the reconstruction probability; $\varepsilon_I = P_a \cdot P_r$ is the efficiency of the structure with two modules and one absorber. The curve ε_{ANC} shows the efficiency of the whole ANC detector.

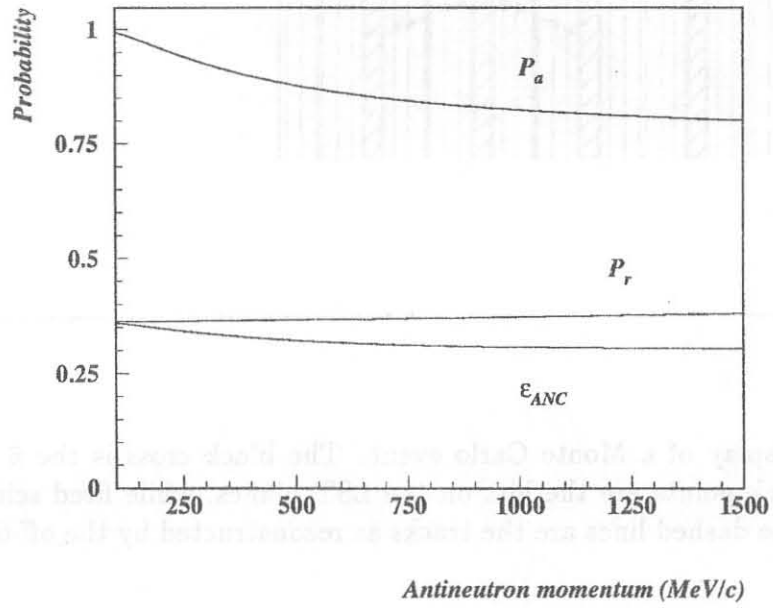

Figure 13: ANC efficiency ε_{ANC} as a function of the $\bar{n}$ momentum. P_a is the $\bar{n}$'s absorption probability in the ANC detector. P_r is the reconstruction probability evaluated using the Monte Carlo program.

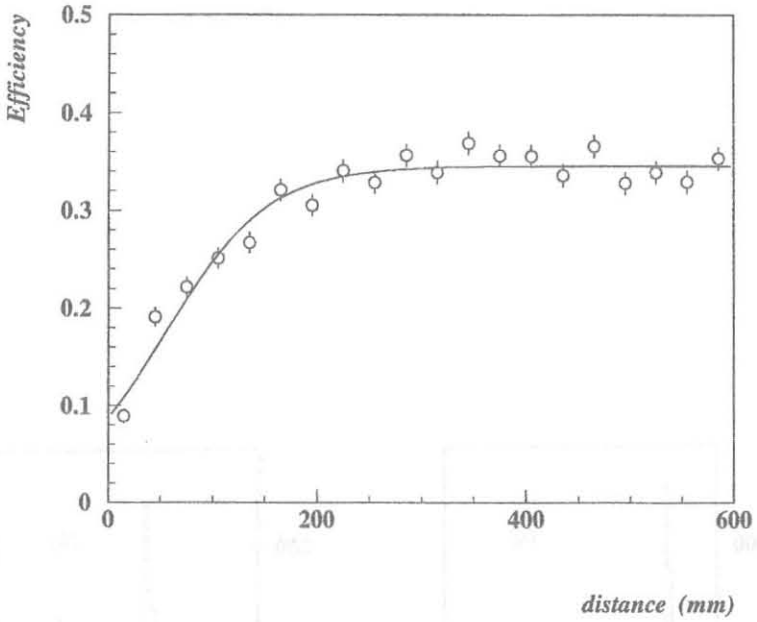

Figure 14: Geometrical acceptance of the ANC as a function of the distance between the edge of the detector and the $\bar{n}$ annihilation point.

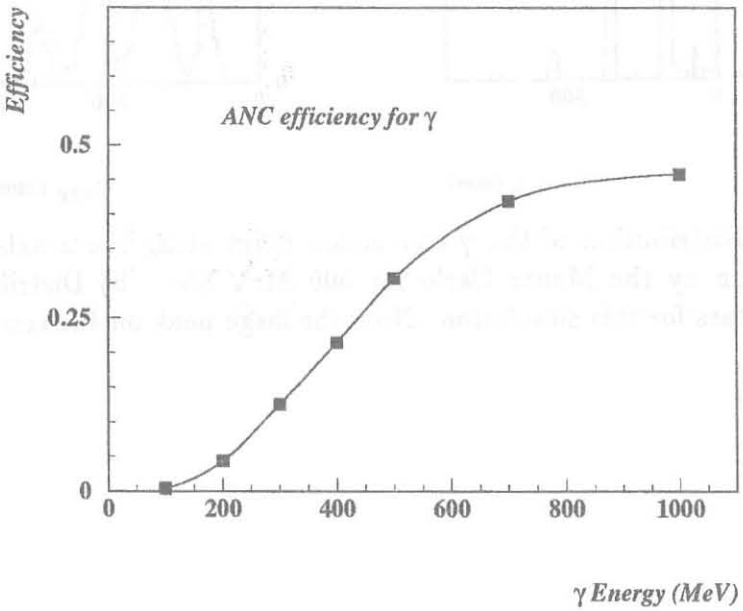

Figure 15: Efficiency of the ANC detector for γ's incoming orthogonally, in the ANC centre, over a large γ energy spectrum.

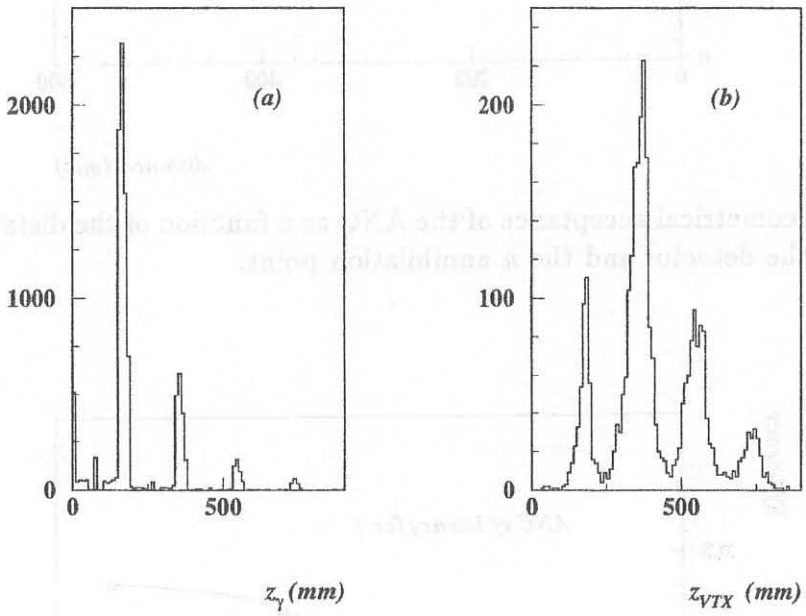

Figure 16: (a) Distribution of the γ conversion point along the z axis of the ANC detector as given by the Monte Carlo for 500 MeV γ's. (b) Distribution of the reconstructed stars for this simulation. Note the large peak on the second absorber.